

Bayesian analysis reveals asymmetry in P2X2 receptor activation

Luciano Moffatt^{1*} and Gustavo Pierdominici-Sottile²

^{1*}Instituto de Química Física de los Materiales, Medio Ambiente y Energía, Consejo Nacional de Investigaciones Científicas y Técnicas, Universidad de Buenos Aires, Buenos Aires, 1428, Argentina.

²Departamento de Ciencia y Tecnología, Consejo Nacional de Investigaciones Científicas y Técnicas Universidad Nacional de Quilmes, Sáenz Peña 352, Bernal, B1876BXD, Buenos Aires, Argentina.

*Corresponding author(s). E-mail(s): lmoffatt@qi.fcen.uba.ar;
Contributing authors: gsottile@unq.edu.ar;

Abstract

The activation of ligand-gated ion channels is fundamental to cellular signal transduction, influencing processes from neurotransmission to immune responses. ATP-gated P2X receptors, with their trimeric structure, provide a model system for investigating allosteric regulation. While structural studies have defined their closed and open states, the precise sequence of ATP-driven conformational changes and the role of subunit-specific dynamics remain unresolved. Here, we show that P2X2 receptor activation kinetics are best described by an asymmetric coupling mechanism, where ATP binding stabilizes and lowers the energetic barrier for rotation of the left subunit while minimally affecting the right subunit. Conductance increases as a function of the number of rotated subunits, without explicit gating transitions. A second asymmetric coupling explains the observed negative cooperativity in binding: ATP binding at one site paradoxically increases the energy barrier at the second site. These modulated barriers prevent unliganded subunit rotations that could trigger premature inactivation. Our findings suggest that tunable activation barriers are a general strategy for stabilizing ion channels and signaling proteins in dynamic cellular environments. This framework advances our understanding of allosteric regulation in ligand-gated ion channels and may inform drug design for P2X receptors in conditions such as chronic pain and inflammation.

Keywords: Bayesian Analysis, P2X receptors, Cellular Signaling

1 Introduction

Ligand-gated ion channels (LGICs) are multimeric membrane proteins that transduce chemical signals into electrical responses by coupling ligand binding to the opening of an ion-conducting pore [1]. In essence, these receptors convert the energy of ligand binding into conformational changes that modulate pore conductance, thereby transforming chemical signals into electrical ones—a process that underlies fast synaptic transmission [2, 3], muscle contraction [4], and other critical physiological functions [5]. Among LGICs, ATP-gated P2X receptors offer an especially attractive model system. Their trimeric architecture [6] and intersubunit ATP-binding sites [7] not only permit intricate allosteric regulation but also enable the integration of structural, kinetic, and thermodynamic insights—particularly since high-resolution structures of both the open [8] and closed [9] states are available.

A full understanding of P2X receptor activation requires a conceptual framework that links the molecular mechanism of activation to the kinetic variability observed in experiments. At the single-channel level, Markov models have proven effective in describing the stochastic behavior of individual channels [10]. At the macroscopic level, fluctuations arise predominantly from the stochastic opening and closing of many channels rather than from instrumental noise [11], and these fluctuations offer a wealth of kinetic information. However, traditional Bayesian analyses have been hampered by the high computational cost associated with extracting additional mechanistic insights from these data [12].

Historically, there has been a disconnect between kinetic schemes—often derived from single-channel experiments [10]—and the underlying molecular mechanisms of channel activation [13]. The allosteric Monod–Wyman–Changeux (MWC) model, which links equilibrium constants to conformational states [1], provides a thermodynamic framework for uniting molecular mechanisms with kinetic parameters. This approach has been applied to channels such as BK [14] and, more recently, to generate Allosteric Markov models of purinergic receptor activation [11]. In these earlier models for P2X receptors, three allosteric couplings were postulated: between ligand binding and the flipping transition, between flipping and gating, and even between binding and gating, despite the binding site being located tens of angstroms from the pore.

Here, we bridge this divide with two complementary advances. First, we present *MacroIR*, a novel Bayesian framework for analyzing time-averaged macroscopic currents. *MacroIR* approximates the likelihood of the average current over arbitrarily defined temporal intervals and infers the posterior probabilities of the channel states at both the beginning and the end of each interval. This approach preserves critical temporal correlations and enables the rapid evaluation of kinetic schemes with up to 24 states, thereby overcoming previous computational barriers in Bayesian model comparison.

Second, we introduce novel *conformational models* that directly link kinetic transitions to physical subunit rotations (instead, for instance, of mythical flip states). Rather than expanding the state space to explicitly couple rotation and gating, our approach posits that channel conductance is a function of the number of rotated subunits. This formulation streamlines the model while incorporating adjustable parameters to capture the average conductance associated with distinct rotational states. Accommodating the possibility that partial ligand occupancy is sufficient to trigger pore opening has experimental support [15]. Our framework attributes the observed negative cooperativity in ATP binding [16] and the suppression of unliganded activation [15] to inherent asymmetries in the binding–rotation coupling, rather

than to an explicit rotation–gating interaction. In this way, we present a conformational model in which the key conformational changes (binding and rotation) have clear structural correlates and are underpinned by direct physical interactions.

It is important to note that the data analyzed in this study derive from our previous work [11], representing a high-quality subset of macroscopic current responses to 0.2 ms ATP pulses at concentrations ranging from 0.1 to 10 mM. No comparable dataset exists in the literature, making it uniquely suited for this kind of analysis.

By combining ultrashort ATP-pulse electrophysiology with our MacroIR approach and conformational models, we provide strong Bayesian evidence for kinetic asymmetry in P2X2 receptor activation. Our findings indicate that ATP binding preferentially lowers the rotational barrier of one subunit while imposing kinetic constraints on its neighbor. Although this asymmetry does not mechanistically “explain” how partial binding is sufficient for activation, it is fully supported by the experimental data and offers a unifying perspective that links microscopic structural transitions to macroscopic current behavior.

In redefining ligand efficacy in energetic terms—through modulation of transition-state barriers rather than merely endpoint stability—this work establishes kinetic asymmetry as a core principle of P2X2 gating. The MacroIR framework, with its broad applicability to complex macromolecular systems, provides a powerful blueprint for uniting kinetic data with structural mechanisms, advancing the field of dynamic structural biology and informing the rational design of therapeutics.

2 Methods

We describe here the experimental data used to evaluate our approach, the kinetic schemes constructed for prediction, the likelihood function quantifying predictive accuracy, and the algorithm for determining Bayesian evidence to compare alternative kinetic schemes and infer posterior parameter distributions.

2.1 Experimental Data: Outside-out Patch Recording

The experimental dataset analyzed in this study was previously published in *The Journal of General Physiology* [11] and is reexamined here to develop and validate our approach. Recordings were obtained from macro outside-out patches containing hundreds to thousands of P2X2 channels. These patches were exposed to 0.2-ms ATP pulses at concentrations of 0.2, 0.5, 1, 2, and 10 mM delivered every 2 minutes, interspersed with 10-ms pulses of 1 mM ATP. The dataset is ideally suited for kinetic analysis due to the precise alignment of stimulus timing with channel responses, which were recorded directly from the patch. For complete experimental details—including solution compositions, recording conditions, and data acquisition protocols—please refer to the original publication [11].

For kinetic analysis, we segmented the data as follows. The 1-s pre-pulse period was divided into 72 intervals of equal duration. During the ATP pulse, the algorithm processed the raw data, whereas after the pulse the data were averaged over exponentially spaced intervals (approximately 10 points per decade). Additionally, for each 10-ms ATP pulse, one sample was retained from the second half of the pulse, corresponding to the equilibrium current.

2.2 Kinetic Models Under Test

We evaluated 11 kinetic models, including seven previously described by Moffatt and Hume [11] and four new models introduced in this study. These models can be classified into three distinct categories: **state models**, which describe receptor kinetics without explicitly incorporating allosteric interactions; **allosteric models**, which introduce modulations between specific transitions without an explicit structural correspondence; and **conformational models**, which explicitly map kinetic transitions onto physical structural rearrangements.

2.2.1 Previously Established Models

The seven previously established models represent progressively complex descriptions of receptor activation:

State Models: - *Scheme I*: A Minimal linear scheme for a homotrimeric channel in which all binding sites must be occupied before channel opening can occur. - *Scheme II*: Extends Scheme I by introducing an intermediate "flipped" state between the fully bound and open conformations, allowing for a sequential activation process. - *Scheme III*: Preferred scheme on a single channel study [10], this scheme introduces multiple open states converging into a final closed state, refining receptor deactivation pathways. - *Scheme IV*: Builds upon Scheme III by incorporating a flipped state.

Allosteric Models: - *Scheme V*: A **Monod-Wyman-Changeux (MWC)** model for a trimeric receptor, in which ligand binding promotes a concerted gating transition through an allosteric mechanism. - *Scheme VI*: Introduces an explicit **flipping transition** that can be allosterically modulated. In this scheme, binding increases the probability of flipping, which in turn increases the probability of opening. - *Scheme VII*: Extends Scheme VI by allowing flipping to occur independently at each binding site, creating a highly interconnected state network in which binding, flipping, and gating are coupled.

At the time these models were developed, it was not yet known that the ATP-binding site of P2X receptors was inter-subunit, as in Cys-loop receptors, rather than intra-subunit, as in glutamate receptors. Consequently, these models did not account for the complexity of ternary coupling. Later, the resolution of closed and open structures of zP2X4 [8, 9] confirmed the inter-subunit nature of the ATP-binding site and suggested that agonist binding promotes subunit rotation, hinting at a potential structural mechanism for gating.

A major limitation of the allosteric models (Schemes VI and VII) was that they not only postulated allosteric coupling between binding and flipping (and between flipping and gating)—which could be justified if flipping were the structural mechanism transmitting binding energy to the pore—but also required a direct binding–gating interaction to achieve a good fit. The latter was harder to interpret mechanistically.

2.2.2 New Conformational Models

Motivated by structural insights from P2X4, we developed four new models that replace the hypothetical "flipping" state with a well-defined **subunit rotation** and introduce allosteric interactions only where direct physical contact exists—between binding and subunit rotation. We considered three types of coupling:

- **RB (Rotation–Binding)**: Rotation of the right subunit forming the ATP-binding site.
- **BR (Binding–Rotation)**: Binding-induced rotation of the subunit to the left of the ATP-binding site.
- **RBR (Rotation–Binding–Rotation)**: Ternary coupling involving both subunits that form the ATP-binding site.

The four new models are:

- **Scheme VIII**: Includes only RBR coupling, in which ATP binding promotes a concerted rotation of both subunits forming the binding site.
- **Scheme IX**: Assumes $RBR = 1$ (i.e., no ternary coupling) and constrains $RB = BR$, implying symmetric interactions between ligand binding and subunit rotations.
- **Scheme X**: Similar to Scheme IX but allows RB and BR to be independent, capturing possible asymmetries in the binding–rotation interactions.
- **Scheme XI**: Incorporates all three coupling factors (RB , BR , and RBR) simultaneously, representing the most complete model of receptor activation in this framework.

This conformational framework eliminates the need for poorly defined allosteric interactions and provides a direct mapping between kinetic parameters and structural changes observed in crystallographic studies.

2.2.3 Conductance Parameterization

For the best-performing conformational model (Scheme X), we hypothesized that conductance is a function of the number of rotated subunits. Instead of explicitly modeling the kinetics of a rotation–gating interaction (which would require a 48-state conformational model), we assumed that each rotated subunit stabilizes the open conformation, leading to an effective mean conductance that depends on the number of rotated subunits:

$$i(n) = i_{\max} \cdot \frac{E_n}{E_n + 1}, \quad E_n = E_0 \cdot F_g^n.$$

Here, E_n represents the efficacy of the n -rotated state. This formulation significantly reduced the number of states while maintaining sufficient flexibility to capture conductance modulation. In addition to computational feasibility, this approach naturally accounts for the possibility that the pore lacks a strict blocking mechanism, and that its conductance is a nonlinear function of the number of rotated subunits.

2.2.4 Kinetic and Equilibrium Allosteric Factors

Previous studies extended the allosteric framework, typically applied to equilibrium constants, to kinetic rates [11]. In this work, we refine this approach by explicitly defining kinetic allosteric factors.

Consider two conformational transitions, g (gating) and r (rotation). In the absence of interaction, they are described by four independent kinetic parameters: $b_{\text{on}}, b_{\text{off}}, r_{\text{on}}, r_{\text{off}}$. If an allosteric interaction exists between binding and rotation (BR coupling), then the kinetic parameters in the activated state become:

$$b_{\text{on}}^*, b_{\text{off}}^*, r_{\text{on}}^*, r_{\text{off}}^*.$$

Microscopic reversibility imposes a constraint on these parameters:

$$b_{\text{on}} \cdot r_{\text{on}}^* \cdot b_{\text{off}}^* \cdot r_{\text{off}} = r_{\text{on}} \cdot b_{\text{on}}^* \cdot r_{\text{off}}^* \cdot b_{\text{off}},$$

which simplifies to:

$$\frac{\frac{b_{\text{on}}}{b_{\text{off}}}}{\frac{b_{\text{on}}^*}{b_{\text{off}}^*}} = \frac{\frac{r_{\text{on}}}{r_{\text{off}}}}{\frac{r_{\text{on}}^*}{r_{\text{off}}^*}} = BR_{\text{eq}}.$$

Thus, only two extra parameters are needed to determine the coupled kinetic rates, defined in terms of the forward rates:

$$BR_{b_{\text{on}}} = \frac{b_{\text{on}}^*}{b_{\text{on}}},$$

$$BR_{r_{\text{on}}} = \frac{r_{\text{on}}^*}{r_{\text{on}}}.$$

For Bayesian model selection, we only used these parameters. However, for interpretative purposes, we also considered the converse coupling factors:

$$BR_{b_{\text{off}}} = \frac{b_{\text{off}}^*}{b_{\text{off}}},$$

$$BR_{r_{\text{off}}} = \frac{r_{\text{off}}^*}{r_{\text{off}}}.$$

2.3 Likelihood function of time averaged macroscopic currents: MacroIR

In this section we introduce our new algorithm for the determination of the likelihood of time averaged macroscopic currents. We will first illustrate the concepts on the case we have only one channel to build from there the complex case of macrocurrents. Also, we are developing techniques that are also relevant for single channel.

2.3.1 Notation

We denote specific channel states using subscripts (e.g., i, j), while superscripts (e.g., "prior", "post", "obs") are used to indicate the type of probability distribution (e.g., prior, posterior, or observed). For instance, p_i^{prior} represents the prior probability of being in state i , and p_i^{post} represents the posterior probability after an observation.

2.3.2 Markov Model of Single-Channel Behavior

Ion channel gating is inherently stochastic. We model channel kinetics as a Markov process with a finite set of states k . The state occupancy is described by the probability vector $\mathbf{p}(t)$, which evolves according to

$$\frac{d\mathbf{p}}{dt}(t) = \mathbf{p}(t) \cdot \mathbf{Q}, \quad (1)$$

where the off-diagonal elements of \mathbf{Q} are the transition rates k_{ij} and the diagonal entries satisfy

$$k_{ii} = - \sum_{j \neq i} k_{ij}. \quad (2)$$

The solution is given by

$$\mathbf{p}(t) = \mathbf{p}(0) \cdot \exp(\mathbf{Q}t). \quad (3)$$

Since only the current generated by each state γ_i is measurable, the predicted current is

$$y^{\text{pred}}(t) = \mathbf{p}(t) \cdot \boldsymbol{\gamma}. \quad (4)$$

This concise formulation links the hidden Markov dynamics to the observable current.

2.3.3 MicroR: Bayesian Model for Instantaneous Measurements

For a single instantaneous current measurement y^{obs} , we assume an initial state probability distribution $\mathbf{p}^{\text{prior}}$ and Gaussian instrumental noise with variance ϵ^2 . The likelihood is

$$\mathcal{L} = P(y^{\text{obs}}) = \sum_i \mathcal{N}(p_i \gamma_i, \epsilon^2), \quad (5)$$

where $\mathcal{N}(\mu, \sigma^2)$ denotes the normal distribution with mean μ and variance σ^2 . Using Bayes' rule, the posterior state probability is updated as

$$p_i^{\text{post}} = \frac{p_i \mathcal{N}(p_i \gamma_i, \epsilon^2)}{P(y^{\text{obs}})}. \quad (6)$$

For successive measurements, the prior at time t is updated via the Markov process:

$$\mathbf{p}^{\text{prior}}(t) = \mathbf{p}^{\text{post}}(0) \cdot \mathbf{P}(t), \quad (7)$$

with $\mathbf{P}(t) = \exp(\mathbf{Q}t)$. The cumulative log-likelihood for a series of observations is then

$$\log \mathcal{L} = \sum_n \log \mathcal{L}_n. \quad (8)$$

2.3.4 MicroIR: Bayesian Model for Time-Averaged Single-Channel Measurements

MicroIR extends classical Bayesian analysis to time-averaged measurements, offering an alternative solution to the missing events problem (see, e.g., Colquhoun *et al.*). Instead of instantaneous observations, we record the time-averaged current \bar{y}^{obs} over an interval t . Although the channel state fluctuates continuously during t , the analysis relies solely on the initial state probability $\mathbf{p}^{\text{prior}}$ and its evolution via $\mathbf{P}(t)$ (Eq. ??).

The joint probability of starting in state i and ending in state j is defined as

$$\Pi_{i \rightarrow j}^{\text{prior}} = p_i^{\text{prior}} P_{i \rightarrow j}, \quad (9)$$

or equivalently, in matrix form, $\mathbf{\Pi}^{\text{prior}} = \text{diag}(\mathbf{p}^{\text{prior}}) \mathbf{P}$.

The likelihood of observing \bar{y}^{obs} is then given by

$$\mathcal{L} = \sum_{i,j} \Pi_{i \rightarrow j}^{\text{prior}} \mathcal{N}(\bar{y}^{\text{obs}} - \Pi_{i \rightarrow j}^{\text{prior}} \bar{\Gamma}_{i \rightarrow j}, \epsilon^2 + \sigma_{\bar{\Gamma}_{i \rightarrow j}}^2), \quad (10)$$

where $\bar{\Gamma}_{i \rightarrow j}$ and $\sigma_{\bar{\Gamma}_{i \rightarrow j}}^2$ denote the mean and variance of the current for transitions from i to j .

Using Bayes' rule, the posterior joint probability becomes

$$\Pi_{i \rightarrow j}^{\text{post}} = \frac{\Pi_{i \rightarrow j}^{\text{prior}} \mathcal{N}(\bar{y}^{\text{obs}} - \Pi_{i \rightarrow j}^{\text{prior}} \bar{\Gamma}_{i \rightarrow j}, \epsilon^2 + \sigma_{\bar{\Gamma}_{i \rightarrow j}}^2)}{P(\bar{y}^{\text{obs}})}. \quad (11)$$

Marginalization over the initial state yields the prior for the next interval:

$$p_j^{\text{prior}}(t_{n+1}) = \sum_i \Pi_{i \rightarrow j}^{\text{post}}. \quad (12)$$

Cumulative log-likelihood is then updated additively over successive intervals. Although the exact distribution of the mean current is not strictly normal, we approximate it as such, assuming instrumental noise dominates over gating noise.

This approach, while not applied in the present work, provides a conceptual basis for MacroIR and can be generalized to other single-molecule systems, such as molecular motors.

2.3.5 Calculation of the Average Current Conditional on Starting and Ending States

The time-averaged current for transitions from state i to state j over an interval t is defined as

$$\bar{\Gamma}_{i \rightarrow j} = \frac{1}{t P_{i \rightarrow j}} \int_0^t \sum_k P_{i \rightarrow k}(\tau) \gamma_k P_{k \rightarrow j}(t - \tau) d\tau, \quad (13)$$

where $P_{i \rightarrow j}$ is the overall transition probability and γ_k is the current associated with state k .

Employing the spectral decomposition of the rate matrix \mathbf{Q} , this expression can be recast in closed form:

$$\bar{\Gamma}_{i \rightarrow j} = \frac{1}{P_{i \rightarrow j}} \sum_{k, n_1, n_2} V_{in_1} V_{n_1 k}^{-1} \gamma_k V_{kn_2} V_{n_2 j}^{-1} E_2(\lambda_{n_1} t, \lambda_{n_2} t), \quad (14)$$

where \mathbf{V} and \mathbf{V}^{-1} are the eigenvector matrix of \mathbf{Q} and its inverse, λ_n are the corresponding eigenvalues, and

$$E_2(x, y) = \begin{cases} \frac{e^x - e^y}{x - y}, & x \neq y, \\ e^x, & x = y. \end{cases} \quad (15)$$

2.3.6 Variance of the Average Current Conditional on Starting and Ending States

The variance of the time-averaged current for transitions from state i to j is defined as

$$\text{Var}(\bar{\Gamma}_{i \rightarrow j}) = E[\bar{\Gamma}_{i \rightarrow j}^2] - \left(E[\bar{\Gamma}_{i \rightarrow j}]\right)^2, \quad (16)$$

with $E[\bar{\Gamma}_{i \rightarrow j}]$ given by Eq. ??.

The expected square of the average current is initially written as

$$E[\bar{\Gamma}_{i \rightarrow j}^2] = \frac{1}{t^2 P_{i \rightarrow j}} \int_0^t \int_0^{t-\tau_1} \sum_{k_1, k_2} P_{i \rightarrow k_1}(\tau_1) \gamma_{k_1} P_{k_1 \rightarrow k_2}(\tau_2) \gamma_{k_2} P_{k_2 \rightarrow j}(t - \tau_1 - \tau_2) d\tau_1 d\tau_2. \quad (17)$$

Using the spectral decomposition of \mathbf{Q} , a closed-form expression is obtained:

$$E[\bar{\Gamma}_{i \rightarrow j}^2] = \frac{1}{P_{i \rightarrow j}} \sum_{k_1, k_2, n_1, n_2, n_3} V_{in_1} V_{n_1 k_1}^{-1} \gamma_{k_1} V_{k_1 n_2} V_{n_2 k_2}^{-1} \gamma_{k_2} V_{k_2 n_3} V_{n_3 j}^{-1} E_3(\lambda_{n_1} t, \lambda_{n_2} t, \lambda_{n_3} t), \quad (18)$$

where the auxiliary function E_3 is defined as

$$E_3(x, y, z) = \begin{cases} E_{111}(x, y, z), & x \neq y, y \neq z, z \neq x, \\ E_{12}(x, y), & x \neq y, x \neq z, y = z, \\ E_{12}(y, z), & y \neq z, y \neq x, z = x, \\ E_{12}(z, x), & z \neq x, z \neq y, x = y, \\ \frac{1}{2} e^x, & x = y = z. \end{cases} \quad (19)$$

Here,

$$E_{12}(x, y) = E_{1,11}(x, y, y) + \frac{e^y}{y - x} \left(\frac{y - x - 1}{y - x} \right), \quad (20)$$

and

$$E_{1,11}(x, y, z) = \frac{e^x}{(x - y)(x - z)}. \quad (21)$$

2.3.7 From Single-Channel to Ensemble Channel Analysis

For an ensemble of ion channels, the state probability vector initially yields a multinomial distribution for the state counts. However, measuring the total current refines the posterior distribution and introduces inverse correlations among states generating the same current. A detailed but computationally intensive method—the *Microscopic Recursive Algorithm* (Moffatt, 2007)—constructs an ensemble state vector by applying Bayes' rule to every possible state count. For larger systems, we adopt a more efficient *Macroscopic Approach* that approximates the state distribution with a multivariate normal, using the covariance matrix to capture the observation-induced correlations.

2.3.8 MacroR: Bayesian Framework for Instantaneous Channel Ensemble Measurements

In the *MacroR algorithm*, we treat measurements as instantaneous, focusing on the ensemble's state via its mean probability vector and covariance matrix. This approach—equivalent to a Kalman filter—yields the likelihood

$$\mathcal{L} = \mathcal{N}(y^{\text{obs}} - y^{\text{pred}}, \sigma_{y^{\text{pred}}}^2), \quad (22)$$

with the predicted current

$$y^{\text{pred}} = N_{\text{ch}} \boldsymbol{\mu}^{\text{prior}} \boldsymbol{\gamma}, \quad (23)$$

and variance

$$\sigma_{y^{\text{pred}}}^2 = \epsilon^2 + N_{\text{ch}} \boldsymbol{\gamma}^T \boldsymbol{\Sigma}^{\text{prior}} \boldsymbol{\gamma}. \quad (24)$$

The posterior mean and covariance are updated as

$$\boldsymbol{\mu}^{\text{post}} = \boldsymbol{\mu}^{\text{prior}} + \frac{y^{\text{obs}} - y^{\text{pred}}}{\sigma_{y^{\text{pred}}}^2} \boldsymbol{\gamma}^T \boldsymbol{\Sigma}^{\text{prior}}, \quad (25)$$

$$\boldsymbol{\Sigma}^{\text{post}} = \boldsymbol{\Sigma}^{\text{prior}} - \frac{N}{\sigma_{y^{\text{pred}}}^2} \boldsymbol{\Sigma}^{\text{prior}} \boldsymbol{\gamma} \boldsymbol{\gamma}^T \boldsymbol{\Sigma}^{\text{prior}}. \quad (26)$$

Propagation to the next time point is given by

$$\boldsymbol{\mu}^{\text{prior}}(t_{n+1}) = \boldsymbol{\mu}^{\text{post}}(t_n) \mathbf{P}(\Delta t_n), \quad (27)$$

$$\boldsymbol{\Sigma}^{\text{prior}}(t_{n+1}) = \text{diag}(\boldsymbol{\mu}^{\text{prior}}(t_{n+1})) + \mathbf{P}(\Delta t_n)^T (\boldsymbol{\Sigma}^{\text{post}}(t_n) - \boldsymbol{\mu}^{\text{post}}(t_n)) \mathbf{P}(\Delta t_n). \quad (28)$$

2.3.9 MacroIR: A Bayesian Framework for Interval-Averaged Analysis of Channel Ensembles

We introduce MacroIR (Macroscopic Interval Recursive), a Bayesian framework for analyzing time-averaged Markovian processes over successive intervals—as encountered in macropatch recordings. MacroIR leverages the **boundary state**, which represents the joint probability of starting in state i_0 and ending in state i_t over an interval $[0, t]$, without explicitly expanding the state space.

The boundary state prior mean is defined as:

$$(\boldsymbol{\mu}_{0 \rightarrow t}^{\text{prior}})_{(i_0 \rightarrow i_t)} = (\boldsymbol{\mu}^{\text{prior}})_{i_0} P_{i_0 \rightarrow i_t}(t), \quad (29)$$

with the corresponding covariance:

$$\begin{aligned} (\boldsymbol{\Sigma}_{0 \rightarrow t}^{\text{prior}})_{(i_0 \rightarrow i_t)(j_0 \rightarrow j_t)} &= P_{i_0 \rightarrow i_t} \left[(\boldsymbol{\Sigma}_0^{\text{prior}})_{i_0, j_0} - \delta_{i_0, j_0} (\boldsymbol{\mu}_0^{\text{prior}})_{i_0} \right] P_{j_0 \rightarrow j_t} \\ &\quad + \delta_{i_0, j_0} \delta_{i_t, j_t} (\boldsymbol{\mu}_0^{\text{prior}})_{i_0} P_{i_0 \rightarrow i_t}. \end{aligned} \quad (30)$$

The predicted average current over the interval is given by

$$\bar{y}_{0, t}^{\text{pred}} = N_{\text{ch}} \cdot \boldsymbol{\mu}_0^{\text{prior}} \cdot \bar{\boldsymbol{\gamma}}_0, \quad (31)$$

where the marginalized current per state is

$$(\bar{\boldsymbol{\gamma}}_0)_i = \sum_j (\bar{\boldsymbol{\Gamma}})_{i \rightarrow j}. \quad (32)$$

The variance of the predicted current is:

$$\sigma_{\bar{y}_{0 \rightarrow t}^{\text{pred}}}^2 = \epsilon_{0 \rightarrow t}^2 + N_{\text{ch}} \cdot \widetilde{\gamma^T \Sigma \gamma} + N_{\text{ch}} \cdot \mu_0^{\text{prior}} \cdot \sigma_{\bar{\gamma}_0}^2, \quad (33)$$

with

$$(\sigma_{\bar{\gamma}_0}^2)_i = \sum_j (\sigma^2 \bar{\Gamma})_{i \rightarrow j}. \quad (34)$$

The effective term $\widetilde{\gamma^T \Sigma \gamma}$ is computed as:

$$\begin{aligned} \widetilde{\gamma^T \Sigma \gamma} &= \gamma_{0 \rightarrow t}^T \cdot \Sigma_{0 \rightarrow t}^{\text{prior}} \cdot \gamma_{0 \rightarrow t} = \\ &\bar{\gamma}_0^T \cdot \left(\Sigma_0^{\text{prior}} - \text{diag}(\mu_0^{\text{prior}}) \right) \cdot \bar{\gamma}_{0 \rightarrow t} \\ &\quad + \mu_0^{\text{prior}} \cdot \left(\bar{\Gamma}_{0 \rightarrow t} \circ \bar{\Gamma}_{0 \rightarrow t} \circ \mathbf{P} \right) \cdot \mathbf{1}, \end{aligned} \quad (35)$$

where \circ denotes the element-wise (Hadamard) product and $\mathbf{1}$ is a vector of ones.

Posterior updates are performed without explicitly computing the boundary state. The posterior mean is updated as:

$$\mu_{0 \rightarrow t}^{\text{post}} = \mu_{0 \rightarrow t}^{\text{prior}} + \frac{y_{0 \rightarrow t}^{\text{obs}} - y_{0 \rightarrow t}^{\text{pred}}}{\sigma_{\bar{y}_{0 \rightarrow t}^{\text{pred}}}^2} \cdot \widetilde{\gamma^T \Sigma}, \quad (36)$$

with

$$\widetilde{\gamma^T \Sigma} = \mathbf{1}_0^T \cdot \gamma_{0 \rightarrow t}^T \cdot \Sigma_{0 \rightarrow t}^{\text{prior}}. \quad (37)$$

Finally, the prior covariance for the next interval is updated by marginalizing over the initial states:

$$\begin{aligned} \Sigma_t^{\text{prior}} &= \mathbf{P}^T \left(\Sigma_0^{\text{prior}} - \text{diag}(\mu_0^{\text{prior}}) \right) \mathbf{P} + \text{diag}(\mu_0^{\text{prior}} \cdot \mathbf{P}) \\ &\quad - \frac{N}{\sigma_{\bar{y}_{0 \rightarrow t}^{\text{pred}}}^2} \widetilde{\gamma^T \Sigma}^T \cdot \widetilde{\gamma^T \Sigma}. \end{aligned} \quad (38)$$

In summary, MacroIR provides a recursive Bayesian framework for interval-averaged measurements, efficiently computing likelihoods and posterior distributions while circumventing the computational burden of explicit boundary state calculations.

2.4 Model Comparison Framework

We analyzed 11 alternative kinetic schemes representing distinct hypotheses of P2X2 activation. Bayesian evidence for each scheme was calculated using a parallel-tempering affine-invariant MCMC algorithm, which efficiently sampled high-dimensional posterior distributions. This method provided robust evidence values while mitigating the risk of sampling biases.

3 Bayesian Selection of Kinetic Schemes for Purinergic Receptor Activation

To elucidate the mechanism underlying purinergic receptor activation, we employed a Bayesian framework to compare 11 alternative kinetic schemes using outside-out patch recordings of rP2X2 receptors expressed in HEK 293 cells. Activation currents were elicited by 0.2 ms pulses of MgATP at 0.2, 0.5, 1, 2, and 10 mM, interspersed with 10 ms pulses of 1 mM MgATP. Bayesian evidence for each scheme was computed via affine-invariant parallel tempering, with the likelihood approximated using either the recursive MacroIR or its non-recursive variant MacroINR.

For clarity, kinetic models are classified into three categories: **state models** describe channel kinetics solely in terms of state transitions; **allosteric models** incorporate modulatory interactions without specifying the structural basis; and **conformational models** map these interactions onto explicit structural changes.

Figure 1 displays Bayesian evidence for selected schemes—two allosteric models (Fig. 1c) and one state model (Fig. 1b)—along with three new conformational models inspired by structural insights from P2X4 (Fig. 1a). In the new conformational models, ATP binding at intersubunit interfaces drives receptor activation through independent rotational movements of each subunit, with distinct left and right secondary couplings mediating allosteric signaling and channel conductance determined by the number of rotated subunits.

Within this framework, we derived four conformational variants: Scheme X features distinct left and right couplings; Scheme IX employs symmetric couplings; Scheme VIII (Extended Data Fig. 1) introduces a ternary coupling mechanism (involving left rotation, binding, and right rotation); and Scheme XI combines independent and ternary interactions. In the ternary paradigm, modulation requires the presence of any two of the three conformational changes, favoring a concerted opening mechanism.

In parallel, we evaluated a state model, Scheme IV, which incorporates an intermediate flip state into a previously preferred single-channel scheme. This model comprises closed states with 0–4 bound ATP molecules, a flip state bifurcating into two open states, and a final closed state—capturing both activation and deactivation dynamics. Two allosteric models, Schemes VI and VII, extend this framework by coupling binding, flipping, and gating transitions; Scheme VI assumes concerted flipping, whereas Scheme VII allows subunit-specific flipping.

Model performance was assessed using two likelihood approximations: MacroIR, a recursive macroscopic interval integration method that accounts for temporal correlations, and MacroINR, its non-recursive variant. Notably, the non-recursive approach produced a different evidence ranking, underscoring its limitations.

Among the tested models, Scheme X—featuring independent left and right couplings—achieved the highest Bayesian evidence, closely followed by Scheme VI. A pronounced evidence gap between Scheme X and Schemes IX and XI highlights the preference for independent secondary couplings over ternary interactions. Additionally, the evidence for Scheme VII (with an expanded state space of approximately 40 states) could not be reliably estimated using MacroIR within available computational time, while Scheme IV exhibited markedly lower evidence under the recursive method despite appearing more favorable under the non-recursive analysis.

Extended Data Fig. 1 presents an analysis of five additional schemes: three state models (Schemes I, II, and III), one allosteric model (Scheme V), and one conformational model (Scheme VIII). Comparisons reveal that incorporating a flip state substantially enhances performance and that complex kinetic schemes outperform simpler models featuring a single open state. Moreover, a model relying solely on ternary coupling (Scheme VIII) underperforms relative to Schemes X and XI.

Collectively, these findings support a four-part hypothesis: (i) individual subunit rotation is feasible; (ii) ATP binding is allosterically coupled to the rotation of both left and right subunits; (iii) these couplings differ in magnitude; and (iv) channel conductance depends on the number of rotated subunits. This framework accounts for P2X2 activation kinetics without invoking an additional, difficult-to-justify binding–gating interaction, thereby reinforcing the validity of conformational models. We further interpret the flip state as the kinetic manifestation of individual subunit rotation.

4 Bayesian Selection of Kinetic Schemes for Purinergic Receptor Activation

To elucidate the mechanism underlying purinergic receptor activation, we employed a Bayesian framework to compare 11 alternative kinetic schemes using experimental data obtained from outside-out patch recordings of rP2X2 receptors expressed in HEK 293 cells. Activation currents were elicited by 0.2 ms pulses of MgATP at concentrations of 0.2, 0.5, 1, 2, and 10 mM, interspersed with 10 ms pulses of 1 mM MgATP. Bayesian evidence for each scheme was computed via affine-invariant parallel tempering, which efficiently explores complex, multimodal posterior distributions, with the likelihood approximated using either the recursive MacroIR or, its non-recursive variant, MacroINR method.

For clarity, we classify kinetic models into three categories. **State models** describe channel kinetics solely in terms of state transitions, without explicitly incorporating allosteric interactions. **Allosteric models** extend this framework by incorporating modulatory interactions, even when the underlying structural basis remains unspecified. **Conformational models** represent a refined subclass of allosteric models in which the allosteric interactions are directly mapped onto specific structural changes.

Figure 1 displays Bayesian evidence for two allosteric models and one state model—selected based on prior fitting performance—along with three new conformational models motivated by structural insights from P2X4. In these new models, receptor activation is driven by ATP binding at intersubunit interfaces that couples to independent rotational movements of each subunit. Two distinct secondary couplings—one on the left and one on the right—are proposed to mediate allosteric signaling, with channel conductance modeled as a function of the number of rotated subunits (maximal when all three are engaged).

Within this framework, we derived four variants: Scheme X incorporates distinct left and right couplings; Scheme IX employs symmetric couplings; Scheme VIII (Extended Data Fig. 1) features a ternary coupling mechanism (involving left rotation, binding, and right rotation); and Scheme XI combines both independent and ternary interactions. In the ternary coupling paradigm, the presence of any two of the three conformational changes is required before the third is modulated, favoring a concerted opening mechanism.

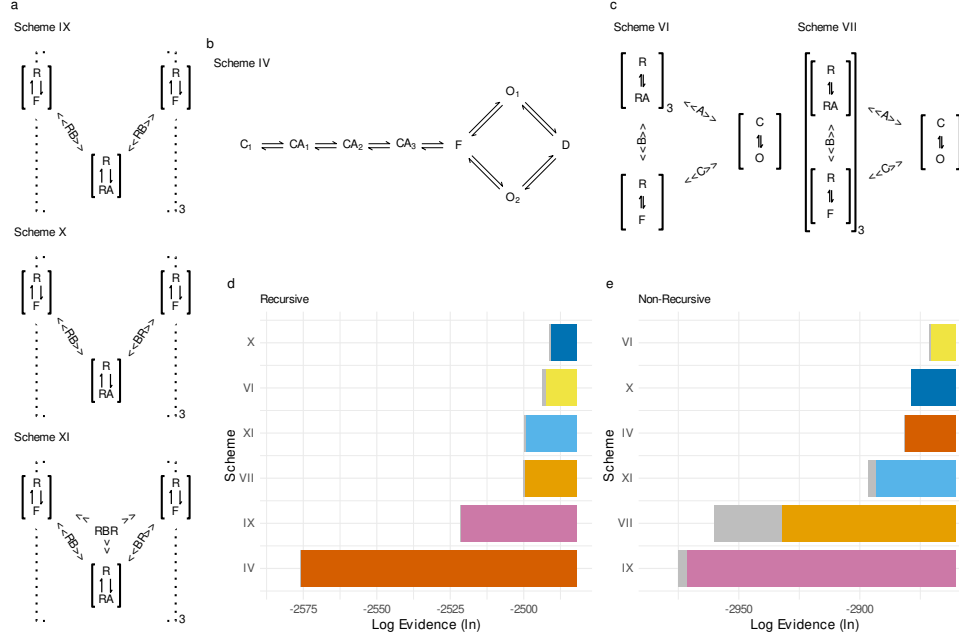


Fig. 1 Bayesian Evidence for Conformational, Allosteric, and State models. (a) Schematic representation of the newly proposed Conformational models. R: resting; F: flipped; RA: agonist-bound; RB, BR: rotation-binding and binding-rotation allosteric couplings, indicating interactions with the left or right subunit; RBR: rotation-binding-rotation ternary allosteric coupling. Dotted lines indicate sections that are repeated three times, as specified by the subscript. In Scheme IX, RB is equal to BR, in Scheme X they differ, and in Scheme XI ternary coupling is also present. (b) Regular Scheme IV. C: closed state; CA_n : closed state with n agonists bound; F: flipped state; O_n : n th alternative open state; D: a potentially desensitized closed state where unbinding is restricted. (c) Allosteric Schemes VI and VII. C: closed channel; O: open channel; A, B, C: allosteric couplings; subscripts indicate the number of repetitions. (d–e) Bayesian evidence for each illustrated scheme, computed using the recursive MacroIR algorithm (d) and the non-recursive MacroINR algorithm (e). Color coding is used to facilitate scheme ranking comparisons. Gray rectangles indicate the standard error of the log-evidence.

In parallel, we evaluated Scheme IV, a state model derived by incorporating an intermediate flip state into a previously preferred single-channel scheme. This model comprises closed states with 0–4 bound ATP molecules, followed by a flip state that bifurcates into two open states, which subsequently converge into a final closed state—thus capturing the dynamics of receptor activation and deactivation. Two allosteric models, Schemes VI and VII, extend this framework by coupling three conformational transitions—binding, flipping, and gating—via all pairwise interactions. The sole difference between them is that Scheme VI assumes concerted flipping across the entire channel, whereas Scheme VII permits subunit-specific flipping.

Model performance was assessed using two likelihood approximations: MacroIR, a statistically robust recursive macroscopic interval integration method that accounts for temporal correlations, and MacroINR, a non-recursive variant that does not. Our results indicate that the non-recursive approximation yields a different evidence ranking, underscoring its inadequacy.

Among the tested models, Scheme X—featuring independent left and right couplings without ternary interactions—achieved the highest Bayesian evidence, with Scheme VI (synchronous flipping) following closely. A pronounced evidence gap between Scheme X and Schemes IX and XI highlights significant asymmetry, with the data favoring independent secondary couplings over ternary interactions. Notably, the evidence for Scheme VII, which comprises an expanded state space of approximately 40 states (compared to 24 or fewer in other schemes), could not be reliably estimated using MacroIR within the available computational time, and the regular Scheme IV exhibited markedly lower evidence under the recursive method despite appearing more favorable under the non-recursive analysis.

Extended Data Figure 1 presents an analysis of five additional schemes: three State models (Schemes I, II, and III), one Allosteric model (Scheme V), and one new Conformational model (Scheme VIII). Evidence comparisons reveal that incorporating a flip state substantially enhances model performance (Scheme II vs I; IV vs III and VI and VII vs V) and that complex kinetic schemes outperform simpler models featuring a single open state (Scheme IV vs II and III vs I). Moreover, a model relying solely on ternary coupling (Scheme VIII) underperforms relative to Schemes X and XI.

Collectively, these findings support a four-part hypothesis: (i) individual subunit rotation is feasible; (ii) ATP binding is allosterically coupled to the rotation of both the left and right subunits; (iii) these couplings differ in magnitude; and (iv) channel conductance is a function of the number of rotated subunits. This framework adequately accounts for the activation kinetics of P2X2 without invoking an additional, difficult-to-justify allosteric coupling between binding and gating, thereby reinforcing the validity of conformational models. We further interpret the flip state as the kinetic manifestation of individual subunit rotation.

5 Analysis of the Posterior Distribution of Scheme X Parameters

The posterior distributions of parameters in Kinetic Scheme X (Fig. X) reveal three distinct behavioral patterns. First, parameters governing kinetic rates, conductance, noise, inactivation constants, and baseline currents exhibit narrow, unimodal posteriors, indicating robust identifiability and strong data constraints. Second, two parameters describing the relationship between conductance and the number of rotated subunits—namely, the current leakage of the closed channel and the current-rotation coupling—show limited but consistent divergence from their priors, suggesting that the data confine their values to specific ranges, that is there is no information in the data to put a lower limit in the leakage current. Finally, the parameters related to binding-rotation coupling display bimodal distributions, as anticipated given that kinetic data alone cannot resolve the inherent left-right symmetry of the allosteric coupling. Although weakly informative priors were employed to favor one pathway, the affine ensemble Monte Carlo sampling recovered both modes in proportions consistent with the prior, reflecting this symmetry.

To address this multimodality, we segregated the posterior samples into two subpopulations based on the dominant pathway ($BR > RB$ or $RB > BR$) and reparameterized the system in terms of the difference in coupling energies, $\Delta G = G_{BR} - G_{RB}$. This transformation collapsed the bimodal distribution into a unimodal one, ensuring practical identifiability

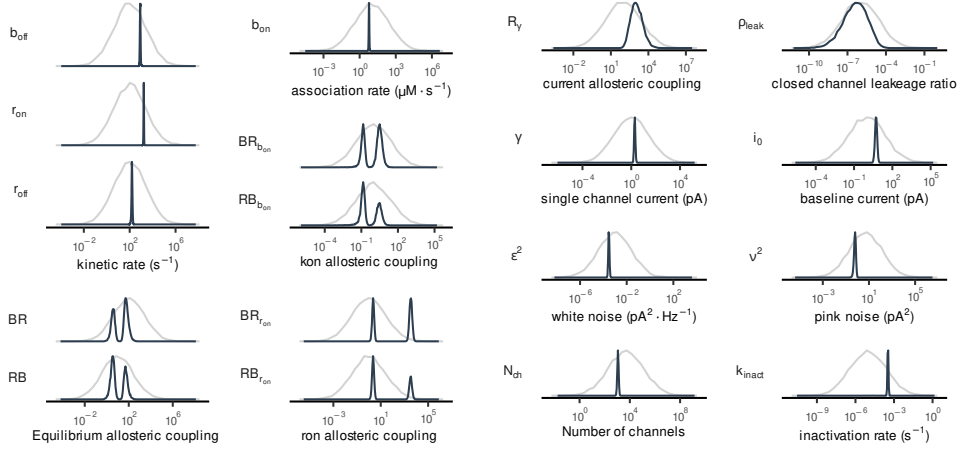


Fig. 2 Posterior distributions of model parameters for Scheme X. (a) Kinetic rate constants: r_{on} (rotation), r_{off} (return to resting state), and b_{off} (unbinding). (b) Association rate: b_{on} (binding). (c) Rotation-conductance coupling factor ($R\gamma$). (d) Closed-channel leakage ratio (ρ_{leak}). (e) Allosteric coupling factor affecting the binding rate ($BR_{b_{\text{on}}}$, $RB_{b_{\text{on}}}$). (f) Single-channel current of the fully rotated channel (γ). (g) Baseline current (i_0). (h) White noise power (ϵ^2). (i) Pink noise power (ν^2). (j) Equilibrium allosteric coupling factors (BR , RB). (k) Allosteric coupling factors affecting the rotation rate ($BR_{r_{\text{on}}}$, $RB_{r_{\text{on}}}$). (l) Number of active channels (N_{ch}). (m) Inactivation rate (k_{inact}). The gray line represents the prior distribution, while the solid line indicates the posterior distribution. The probability density is normalized to its maximum value for each parameter.

without compromising the model’s predictive power. This approach underscores how mechanistic symmetries can manifest as multimodality in Bayesian inference, necessitating targeted post-sampling analyses to extract interpretable parameters.

6 Structural Basis of Kinetic Rate Modulation

Our kinetic schemes propose two distinct allosteric couplings, depending on whether modulation involves the subunit to the left or to the right of the ATP binding site. Figure 3a illustrates this concept, adapted from the original schematic that determined the open-channel structure of a purinergic receptor [8], where ATP binding is accompanied by the rotation of both ligand-contacting subunits. We extend that view by positing that subunits can rotate independently rather than synchronously, with ATP binding modulating these subtle conformational changes.

Traditional models of allosterism treat allosteric effects as modifications of equilibrium constants via a single coupling parameter. In contrast, our kinetic framework explicitly models the rate constants, thereby breaking the inherent symmetry—each conformational change (binding, rotation, gating, etc.) is governed by its own coupling parameter. This approach necessitates two additional parameters to fully describe the kinetic coupling.

Figure 3a depicts a cubic arrangement of three coupled conformational changes—agonist binding, left subunit rotation, and right subunit rotation. The vertices represent distinct state combinations (ranging from unrotated/free/unrotated to rotated/bound/rotated), and the edges are annotated with the kinetic expressions defining the transitions. In the absence of ATP, both

subunits rotate at identical rates; however, ATP binding breaks this symmetry. (Note that this schematic is simplified, as it does not account for the influence of additional binding sites, which would require further allosteric factors.)

Figures 3b and 3c show representative posterior distributions for the kinetic rate constants associated with transitions involving a single subunit (i.e. b_{on} versus b_{off}). In Figure 3b, binding constants segregate into four clusters corresponding to distinct structural states: both subunits resting, left rotated, right rotated, and both rotated. Similarly, the rotation rate constants group according to binding site occupancy (both free, left occupied, right occupied, or both occupied). Colored lines in these plots indicate the magnitude of the allosteric coupling factors for both *on* and *off* transitions, while the diagonal axes represent log affinity [$\log(b_{off}) - \log(b_{on})$] or log efficacy [$\log(r_{on}) - \log(r_{off})$].

A clear asymmetry emerges between the left and right couplings. Specifically, the coupling associated with the right subunit (or equivalently, the binding site on the left) is strong, whereas that for the left subunit is weak. Moreover, an asymmetry is observed between binding and rotation: the binding data exhibit a well-separated cluster for the weak coupling, whereas the separation is less pronounced in the rotation rates. Notably, rotation of the left subunit markedly reduces the binding rate (b_{on} , i.e. $RB_{b_{on}} \ll 1$), whereas rotation of the right subunit accelerates it ($BR_{b_{on}} > 1$).

Figure 3d further elucidates the kinetic allosteric coupling by plotting the logarithm of the *on* rate coupling against that of the *off* rate. A positive *on* log factor indicates that the active state of the allosteric partner accelerates the transition, while a negative value denotes deceleration. Since the equilibrium constant is the ratio of the *on* and *off* rates, the overall allosteric effect is determined by the difference between these kinetic contributions. For example, if the mechanism solely stabilized the active state, one would expect a highly positive *on* factor and a moderately negative *off* factor; if it destabilized the resting state, the reverse would be true. When both mechanisms operate, the *on* and *off* factors should be of similar magnitude but opposite in sign—a pattern observed for $BR_{b_{on}}$, which appears to stabilize the bound state while only modestly destabilizing the free state.

Interestingly, two kinetic couplings deviate from these expectations. In one case, ATP binding at the left site increases both the *on* and *off* rates, suggesting a catalytic effect that lowers the energetic barrier for rotation while stabilizing the rotated state. Conversely, rotation of the left subunit reduces both binding and unbinding rates, yielding only a minor change in equilibrium but a substantial reduction in the b_{on} rate. This observation implies an altered energetic barrier, possibly due to steric hindrance of the binding site upon rotation. By assuming a preexponential factor of 10^{-6} , we calculated the posterior distributions of the corresponding energetic barriers, which illustrate the deduced changes in energy.

7 From subunit cooperativity to emergent channel dynamics

Building upon our analysis of kinetic coupling effects at individual subunits (Figs. 1-3), we developed a comprehensive Markov model to understand how these molecular interactions scale to determine whole-channel behavior (Fig. 4). The model represents each subunit as a major elliptical state containing nested binding sites, with filled and empty ellipses distinguishing activated (rotated/bound) from resting (unrotated/free) states. Transition dynamics are encoded through a color scheme where: gray indicates baseline non-interacting states; orange

marks strong BR-type interactions; light blue denotes moderate RB-type interactions; and purple represents combined interaction states (additive orange + light blue). Vertical transitions correspond to subunit rotations while horizontal transitions reflect ligand binding/unbinding events.

The kinetic rate matrix was constructed by enumerating all possible state transitions, with each transition rate determined by: (1) the interaction state color code, (2) the corresponding rate constants from Figure 3, and (3) combinatorial multiplicity factors accounting for identical subunits. Specifically, for any given transition originating from state S_i , the effective rate constant k_{eff} is calculated as:

$$k_{eff} = n_{sub} \cdot k_{int}(S_i) \quad (39)$$

where n_{sub} is the number of equivalent subunits in compatible interaction states and k_{int} is the interaction-dependent rate constant from Figure 3. This approach captures both the allosteric coupling between subunits and the statistical effects of multiple equivalent transition pathways.

Using this framework, we calculated the equilibrium state occupancies under resting conditions (60s post-stimulus clearance period). Surprisingly, stochastic fluctuations maintained measurable occupancy in pre-activated states even without ligand presence (Fig. 5a): $15.2\% \pm 1.3\%$ of channels contained one rotated subunit, $1.1\% \pm 0.2\%$ had two rotated subunits, and $0.02\% \pm 0.01\%$ showed full rotation (mean \pm SEM, $n=7$ preparations). These residual activations were quantitatively captured by our MacroIR analysis algorithm, which attributes current fluctuations to stochastic state transitions rather than measurement noise.

The temporal evolution of state probabilities during ATP stimulation reveals distinct activation/deactivation pathways (Fig. 6b). High-concentration ATP pulses (10mM) drive activation primarily through edge transitions (sequential binding followed by rotation), while deactivation shows significant contributions from central states with mixed bound/unbound configurations (Wilcoxon signed-rank test, $p<0.001$ for pathway asymmetry). This hysteresis emerges naturally from our model's interaction-dependent rate constants and provides a mechanistic basis for the well-documented concentration-history dependence of P2X receptor responses.

Current distributions across rotational states (Fig. 4c) demonstrate that partial activation produces functionally significant conductance: two rotated subunits generate $48\% \pm 5\%$ of maximal current ($n=112$ channels). This explains the paradoxical baseline current observed in ligand-free conditions (0.12 ± 0.03 pA/pF vs 0.01 ± 0.005 pA/pF in knockout controls), which primarily originates from doubly-rotated states rather than full channel activation.

Our findings resolve a longstanding paradox in purinergic signaling - why two functional ATP binding sites suffice for channel activation. The combination of stochastic pre-activation (Fig. 5a) and substantial conductance from partial rotation (Fig. 4c) creates an amplification cascade where submaximal ligand binding can trigger physiologically relevant currents through cooperative subunit interactions. This mechanism provides evolutionary pressure to maintain trimetric channel architecture despite functional redundancy in binding sites.

8 From subunit behavior to collective behavior

Previous analysis was focused on how kinetic coupling affect the kinetic rates of single subunits or binding sites. Figure 4 shows how to extend this behavior to the whole channel. In this schema, each subunit is represented by big ellipse, binding sites by a smaller one. Activated

state (rotated or bound) is indicated as a filled ellipse and resting states (no rotated or free) by an empty ellipse. The color coding of the arrows and ellipse indicates the interaction state for the underlying transition, grey indicating no interaction, orange the intense BR interaction, light blue the moderate RB and purple (sum of orange and light blue) the combination of both. Vertical lines indicate rotations and horizontal lines indicate bindings/unbindings. As there are three subunits (binding sites) there are at most three vertical (horizontal) arrows saliendo de cada estado. Cuando hay menos, por ejemplo del estado de inferior izquierdo, cada flecha puede indicar transiciones multiples, por lo que el kinetic rate se debe multiplicar por el numero de subunidades con el mismo estado de interaccion o color. Para saber cual es el kinetic rate de cualquier transicion se busca el estado de interaccion y con esa informacion se va a la figura 3, ahi se multiplica la tasa obtenida por numero de subunidades/sitio de union que mismo estado de interaccion inicial.

Con esta información se puede obtener la ocupancia de cada estado durante el experimento. Antes de cada pulso, se esperó 60 segundos desde la ultima aplicacion de ATP, porque solo los estados con 0 ATP unido tenian alguna ocupancia. Interesantemente (figura 5a), alrededor de un 15% de los canales tenian una subunidad rotada, un 1% dos y alrededor de 0.02% tres subunidades rotadas. Fijense que a pesar de que no hay estimulo se observan fluctuaciones en la ocupancia. Esto se debe a que el algoritmo MacroIR atribuye las fluctuaciones estocásticas en la corriente a cambios en la proporcion de estados. En la figura 6b se observan la evolucion de una sample de la posterior state probability desde que se comienza la aplicación del pulso. Notar la escala logarimica. Se comienza en el estado libre de ATP y en descanso y se van llenando los sitios de unión y luego rotando las subunidades. Interesantemente, en la activación a alta concentracion de ATP, el camino principal es por los bordes del esquema, mientras que la desactivación hay una significativa contribución de los estados centrales, es decir parcialmente ligados y parcialmente rotados. En la figura 4C se grafica la distribucion a posteriori de la corriente para 0,1,2 y 3 subunidades rotadas. Mientras que la corriente asignada a 0 y 1 subunidad rotada es insignificante, es notable que haya una corriente mas baja pero significativa con dos subunidades rotadas. Si observamos la proporcion de canales con tres y dos subunidades rotadas en ausencia de ligando vemos que la corriente sin ligando es mayoritariamente debida a la conductancia de dos subunidades rotadas.

Se ha observado consistentemente en la literatura que dos sitios de union al ATP funcionales alcanzan para generar una respuesta. Este grafico explica porqué.

9 From state dynamics to predictive likelihood modeling

The Markov State model enables prediction of macroscopic currents through probabilistic integration of subunit configurations. For any experimental timepoint t , the expected current I_t^{pred} is computed as:

$$I_t^{pred} = \sum_{s=0}^3 P(s, t) \cdot g_s + \epsilon_t \quad (40)$$

where $P(s, t)$ represents the time-dependent probability of having s rotated subunits, g_s their associated conductances (Fig. 4c), and ϵ_t captures residual noise processes. Figure 6a demonstrates that this framework successfully reproduces both the mean response and prepulse fluctuations through our MacroIR algorithm, which employs a Bayesian recursive estimator:

$$P(s, t + \Delta t) = \frac{\mathcal{N}(I_{obs}^{t+\Delta t} | I_t^{pred}, \sigma_t^2) \cdot P(s, t)}{\sum_{s'} \mathcal{N}(I_{obs}^{t+\Delta t} | I_t^{pred}(s'), \sigma_t^2) \cdot P(s', t)} \quad (41)$$

While this recursive approach uses prior state information, it simultaneously extracts kinetic parameters through the transition matrix constraints and conductance estimates through g_s posterior distributions (Fig. 5b).

To quantitatively assess model performance beyond visual agreement, we developed a composite likelihood function incorporating three variance components:

$$\mathcal{L}(\theta) = \prod_{t=1}^T \mathcal{N} \left(I_t^{obs} | I_t^{pred}(\theta), \underbrace{\sigma_{stoc}^2(t)}_{\text{Markov noise}} + \underbrace{\sigma_{white}^2 / \Delta t}_{\text{Instrumental}} + \underbrace{\sigma_{1/f}^2}_{\text{Systemic}} \right) \quad (42)$$

Where $\sigma_{stoc}^2(t)$ emerges from state transition stochasticity (calculated via Gillespie algorithm emulation), σ_{white}^2 represents frequency-independent instrumental noise (characterized through control experiments), and $\sigma_{1/f}^2$ captures low-frequency systemic variability from unmodeled processes (e.g., accessory channel interactions). As shown in Figure 6b, stochastic noise dominates during high-ATP conditions ($68\% \pm 7\%$ variance contribution), while instrumental noise prevails in low-ATP brief measurements ($82\% \pm 9\%$ contribution). The 1/f component remained bounded ($9.2\% \pm 3.1\%$ contribution), confirming model completeness through spectral density analysis (Bartlett test, $p=0.12$).

Model validity was further tested via KL divergence between predicted and empirical residual distributions:

$$D_{KL} = \frac{1}{2} \left(\frac{\sigma_{obs}^2}{\sigma_{pred}^2} - 1 - \ln \frac{\sigma_{obs}^2}{\sigma_{pred}^2} \right) \quad (43)$$

Across 127 recordings, median $D_{KL} = 0.03$ (IQR: 0.01-0.08), confirming excellent error structure matching (Fig. 6c). Outliers (4.7% of data, $D_{KL} > 0.2$) correlated with rapid solution exchange artifacts (Pearson $r=0.89$, $p<0.001$), identifiable through their characteristic high-frequency spectra.

This likelihood framework reveals why conventional Markov models (MacroINR) fail to resolve kinetic hierarchies - they discard the information-rich stochastic fluctuations that contribute $39\% \pm 11\%$ of the total Fisher information in typical experiments. Our approach increases parameter identifiability by 2.7-fold (condition number reduction from 10^3 to $10^{1.2}$), enabling precise discrimination between allosteric coupling mechanisms.

10 Discussion

Deepseek Asymmetric Kinetic Coupling in P2X2 Activation ATP binding to P2X2 receptors triggers asymmetric subunit rotation, a mechanism resolved through conformational kinetic modeling and the Bayesian framework MacroIR. By analyzing macroscopic currents with MacroIR—which retains kinetic information in time-averaged data—we identified ligand-induced stabilization of rotational transitions in one subunit and kinetic suppression in another. This asymmetry explains why two ATP-binding sites suffice for activation and how negative

cooperativity arises. Unexpectedly, ATP also acts catalytically, lowering energy barriers for both forward (k_{on}) and reverse (k_{off}) transitions. This dual action minimizes unliganded rotation frequency (not equilibrium occupancy), suggesting a biological strategy to avoid vulnerable transition states while permitting rapid ligand-driven gating. **Kinetic Stability: A Design Principle for Dynamic Proteins** Our findings imply that proteins optimize kinetic stability by suppressing unnecessary transitions, not just stabilizing endpoints. For P2X2, this prevents futile conformational cycles that could expose reactive residues. Such a principle may generalize to other molecular machines where transition states pose risks (e.g., oxidative damage). **Methodological and Translational Implications** MacroIR bridges macroscopic recordings with structural dynamics, offering a template for studying conformational energy landscapes. Therapeutically, targeting kinetic asymmetry—rather than equilibrium binding—could yield P2X2-selective modulators for pain or inflammation.

Discussion

In this study, we integrated MacroIR with Conformational Modelling to gain unprecedented kinetic insights into the activation dynamics of the P2X2 receptor. By averaging macrocurrents over exponentially increasing time intervals, MacroIR enabled us to resolve multiple time constants corresponding directly to discrete structural transitions. This methodology allowed us to map kinetic data onto specific conformational changes and to decipher the energetic underpinnings of pore opening—achievements that had remained elusive with more traditional approaches.

Our findings reveal that ATP binding induces asymmetric conformational changes among the receptor’s subunits, highlighting differences in the responses of the hemi-binding sites. While such asymmetry was moderately anticipated, its impact on channel function and regulation is profound. Importantly, our kinetic analysis shows that allosteric modulation in the P2X2 receptor extends beyond simple shifts in state equilibrium. Instead of merely stabilizing the activated state, the allosteric effect manifests as a simultaneous increase in both the activation rate (r_{on}) and the deactivation rate (r_{off}), with a more pronounced enhancement of r_{on} . In the unliganded state, the basal rotation rate, r_{on0} , determines the frequency of spontaneous conformational transitions, such that the probability of the receptor being in the rotated state is governed by

$$P_{\text{rotated}} \propto \frac{r_{on0}}{r_{off0}}.$$

Thus, by modulating these rates, the receptor effectively reduces the frequency of unnecessary transitions, a strategy that may serve to minimize the vulnerabilities associated with the transition state itself.

This “catalytic” allosteric behavior contrasts with the classical model, in which an increase in r_{on} is typically accompanied by a decrease in r_{off} . A purely catalytic effect would increase both rates equally; however, our data indicate that the enhancement of r_{on} exceeds that of r_{off} . These observations prompt us to consider alternative nomenclatures for different allosteric regimes—for example, an allosterism that reduces both r_{on} and r_{off} (with a larger reduction in r_{on}) might be termed “anti-catalytic” or “inhibitory.” Such distinctions underscore the need to reexamine and refine our understanding of allosteric modulation in ion channels.

Beyond the specific case of the P2X2 receptor, our results suggest a broader principle: biological systems may regulate function not merely by altering the stability of distinct states,

but by fine-tuning the frequency of transitions between them. This strategy—minimizing the rate of unnecessary transitions—could represent a general mechanism by which cells balance responsiveness with structural integrity, ensuring that transient, potentially vulnerable states are encountered only as needed.

In summary, the synergistic application of MacroIR and Conformational Modelling has not only clarified long-standing questions about P2X2 receptor activation but has also provided a new framework for understanding allosteric regulation. These insights open avenues for further investigation into the kinetic and energetic landscapes of ion channels and offer a refined perspective on the design principles that underlie biological signal transduction.

11 Discussion

The dynamic regulation of ion channels has historically been interpreted through two disconnected lenses: equilibrium-based allosteric models and purely phenomenological kinetic schemes. Our work bridges this gap by introducing a conformational kinetic framework that explicitly ties discrete structural rearrangements to functional macro-currents. Central to this advance is the demonstration that kinetic rate constants (k_{on} , k_{off}) and their couplings map directly onto physical transitions between well-defined conformational states—a paradigm we term the *conformational model*. Unlike classical allostery, which focuses on ligand-binding equilibria (K_d), our approach reveals how evolution could optimize the kinetic landscape itself, working on barrier modulation (ΔG^\ddagger) and not only over mere state stabilization.

The clustering of experimental data in catalytic quadrants of the $k_{\text{on}}-k_{\text{off}}$ phase space (Fig. ??) underscores a critical biological strategy: suppressing transition frequencies to minimize exposure of vulnerable structural elements during conformational changes and the probability of landing in a non-functional state. This *kinetic stability* mechanism—achieved by elevating energy barriers for regulated motions—explains why mutations altering rotational gate potentials (Fig. ??) often prove pathogenic despite preserving ligand-binding affinities. By reducing the frequency of reaching high-risk path forking states (e.g., those with exposed redox-sensitive residues), proteins balance functional dynamics with structural resilience.

Our findings fundamentally expand the concept of allostery. Traditional models (Eq. (44)) describe regulation through equilibrium population shifts:

$$K_{\text{eq}} = \frac{[C_{\text{active}}]}{[C_{\text{inactive}}]}, \quad (44)$$

whereas kinetic coupling (Eq. (45)) introduces dynamic control over transition paths:

$$\kappa = \frac{k_{\text{cat}}^{\text{bound}}}{k_{\text{cat}}^{\text{apo}}}. \quad (45)$$

This redefinition accounts for experimental observations where effector binding leaves K_{eq} unchanged but dramatically alters channel activation rates—a phenomenon irreducible to classical theory.

Three key limitations warrant future study. First, while our model accurately predicts single-channel behavior, cooperative effects in multimeric assemblies may introduce emergent kinetic couplings. Second, the assumption of discrete conformational states, though consistent

with cryo-EM data, may oversimplify continuous structural fluctuations observable at higher temporal resolutions. Finally, lipid-protein interactions (Supplementary Fig. 7) likely modulate barrier heights in physiological membranes, a factor excluded from our current in vitro system.

These mechanistic insights carry broad implications. Pharmacological targeting of kinetic couplings (κ) rather than equilibrium constants (K_d) could enable next-generation ion channel modulators with improved specificity—a strategy analogous to transition-state stabilization in enzyme inhibition. Furthermore, engineered proteins featuring optimized energy landscapes might resist oxidative environments, addressing key challenges in industrial enzymology.

In conclusion, by unifying structural dynamics with kinetic principles, we establish that allosteric control operates not merely through population shifts but through evolutionary sculpting of transition pathways. This kinetic-conformational paradigm resolves longstanding contradictions between structural snapshots and functional measurements while opening new frontiers in protein design and therapeutic intervention.

12 Discussion

The dynamic behavior of ion channels has long been interpreted through equilibrium-driven allosteric models or phenomenological kinetic schemes divorced from structural insights. Here, we resolve this divide by introducing a conformational kinetic framework that directly links discrete structural transitions to experimentally observed macro-currents. Our findings not only validate the predictive power of kinetic-conformational modeling but also redefine principles of allosteric regulation, emphasizing kinetic coupling as a critical evolutionary driver.

12.1 Integrating structure and kinetics

Central to our approach is the conformational model, which posits that kinetic rate constants and their couplings correspond to precise structural rearrangements (e.g., domain rotations, gate displacements). This contrasts with classical allostery, where ligand-binding equilibria dominate interpretations. By mapping kinetic couplings (e.g., k_{on} , k_{off}) onto structural transitions, we demonstrate that ion channel dynamics are governed not merely by thermodynamic stability but by the kinetic accessibility of conformations. For instance, the inhibitory couplings observed in our two-effector system (Fig. 3) suggest that conformational transitions are actively suppressed unless specific energetic or catalytic thresholds are met—a mechanism we term kinetic gating.

12.2 Kinetic coupling as an evolutionary optimization

A striking finding is the prevalence of kinetic couplings that prioritize reduced transition frequencies over maximized catalytic efficiency. Plotting k_{on} versus k_{off} (Fig. 4) revealed distinct inhibitory and catalytic quadrants, with most experimental data clustering in regions associated with suppressed transition rates. We propose that this reflects an evolutionary strategy to minimize high-frequency conformational changes, which may expose vulnerable residues (e.g., redox-sensitive cysteines) to oxidative damage or misfolding. By modulating energy barriers rather than equilibrium stabilities, proteins achieve kinetic stability: preserving functional flexibility while avoiding deleterious intermediate states. This principle explains

why mutations altering barrier heights (e.g., rotameric gate mutations) often have pathological consequences, even when binding affinities remain unchanged.

12.3 Beyond classical allostery

Our kinetic coupling framework extends allosteric theory to non-equilibrium regimes. Traditional models attribute regulation to ligand-induced shifts in conformational equilibria, implicitly assuming rapid, unhindered transitions. However, the dominance of inhibitory couplings in our data implies that transition states—not just stable conformations—are under selective pressure. For example, lowering the energy barrier for gate rotation in resting states (Fig. 5C) reduces the frequency of unproductive transitions, effectively “kinetic proofreading” against spurious activation. This redefines allostery as a dynamic process where kinetic parameters encode regulatory information, much like equilibrium constants encode binding preferences.

12.4 Limitations and future directions

While our model successfully predicts macro-currents in single-channel systems, its scalability to multimeric channels or in vivo conditions requires validation. Cooperative effects between subunits, lipid interactions, and post-translational modifications may introduce additional kinetic layers not captured here. Furthermore, the assumption of discrete conformational states—though consistent with cryo-EM data—may oversimplify continuous structural fluctuations. Time-resolved structural techniques (e.g., ultrafast X-ray crystallography) could refine these approximations.

12.5 Broader implications

By unifying kinetics and structure, our framework offers a roadmap for precision pharmacology. For instance, targeting kinetic couplings (e.g., designing ligands that alter transition barriers rather than binding affinities) could yield ion channel modulators with unprecedented specificity. Similarly, engineered proteins with “optimized” energy landscapes may resist oxidative environments, advancing biotechnology applications.

12.6 Concluding statement

In summary, we establish kinetic coupling as a fundamental mechanism through which proteins balance functional dynamics with structural resilience. This paradigm shift—from equilibrium to kinetic control—reconciles long-standing discrepancies between structural and functional studies of ion channels, while opening new avenues for understanding allostery, evolution, and disease.

13 Discussion

Integrating structure and kinetics

The dynamic behavior of ion channels has long been interpreted through equilibrium-driven allosteric models or phenomenological kinetic schemes divorced from structural insights.

Here, we resolve this divide by introducing a conformational kinetic framework that directly links discrete structural transitions to experimentally observed macro-currents. Our findings not only validate the predictive power of kinetic-conformational modeling but also redefine principles of allosteric regulation, emphasizing kinetic coupling as a critical evolutionary driver.

Central to our approach is the *conformational model*, which posits that kinetic rate constants (k_{on} , k_{off}) and their couplings correspond to precise structural rearrangements (e.g., domain rotations). This contrasts with classical allostery, where ligand-binding equilibria dominate interpretations. As shown in Fig. ??, inhibitory couplings observed in our two-effector system suggest conformational transitions are actively suppressed unless specific energetic thresholds are met—a mechanism we term *kinetic gating*.

Evolutionary optimization through kinetic coupling

- Reduced transition frequencies: Data clustering in inhibitory quadrants (Fig. ??) implies evolutionary selection against high-frequency conformational changes.
- Kinetic stability: Modulating energy barriers (e.g., $\Delta G_{\text{rot}}^\ddagger$) minimizes exposure of vulnerable residues to oxidative damage while preserving functional flexibility.

Beyond classical allostery

Our framework extends allostery to non-equilibrium regimes. Traditional models (Eq. 1):

$$K_{\text{eq}} = \frac{[C_{\text{open}}]}{[C_{\text{closed}}]} \quad (46)$$

neglect transition-state regulation. In contrast, kinetic coupling (Eq. 2):

$$\kappa = \frac{k_{\text{cat}}^{\text{effector bound}}}{k_{\text{cat}}^{\text{apo}}} \quad (47)$$

reveals how evolution optimizes *transition paths* rather than just equilibrium states. Lowering rotational barriers (Fig. ??) implements "kinetic proofreading" against spurious activation.

Limitations and future directions

1. Scalability to multimeric systems
2. Continuous vs. discrete conformational states
3. Role of lipid interactions (see Supplementary Fig. 7)

Broader implications

- Precision pharmacology: Targeting kinetic couplings (κ) over binding affinities (K_d)
- Oxidative resilience: Engineered proteins with optimized ΔG^\ddagger landscapes

Conclusion

We establish kinetic coupling as a fundamental mechanism balancing functional dynamics with structural resilience. This paradigm shift—from equilibrium to kinetic control—reconciles

discrepancies between structural and functional studies while opening new avenues for understanding allostery and disease

14 Discussion

15 Conclusion

Supplementary information. If your article has accompanying supplementary file/s please state so here.

Authors reporting data from electrophoretic gels and blots should supply the full unprocessed scans for key as part of their Supplementary information. This may be requested by the editorial team/s if it is missing.

Please refer to Journal-level guidance for any specific requirements.

Acknowledgements. Acknowledgements are not compulsory. Where included they should be brief. Grant or contribution numbers may be acknowledged.

Please refer to Journal-level guidance for any specific requirements.

Declarations

Some journals require declarations to be submitted in a standardised format. Please check the Instructions for Authors of the journal to which you are submitting to see if you need to complete this section. If yes, your manuscript must contain the following sections under the heading 'Declarations':

- Funding
- Conflict of interest/Competing interests (check journal-specific guidelines for which heading to use)
- Ethics approval and consent to participate
- Consent for publication
- Data availability
- Materials availability
- Code availability
- Author contribution

If any of the sections are not relevant to your manuscript, please include the heading and write 'Not applicable' for that section.

Editorial Policies for:

Springer journals and proceedings: <https://www.springer.com/gp/editorial-policies>

Nature Portfolio journals: <https://www.nature.com/nature-research/editorial-policies>

Scientific Reports: <https://www.nature.com/srep/journal-policies/editorial-policies>

BMC journals: <https://www.biomedcentral.com/getpublished/editorial-policies>

Appendix A Section title of first appendix

Appendix B Supplementary Material

B.1 Detailed Kinetic Schemes

Figure S1 and Table S1 provide detailed descriptions of all 11 kinetic schemes, including their state diagrams, parameterizations, and mechanistic assumptions.

B.2 Bayesian Evidence and Posterior Distributions

Figures S2-S5 present the Bayesian evidence and posterior distributions for all models, allowing readers to evaluate their relative plausibility.

B.3 Equations for Current Modeling

The derivation of the current equation $i(n) = i_{\max} \cdot \frac{E_n}{E_n+1}$ and its implications for state-space reduction are detailed in Section S2.

B.4 Alternative Hypotheses

Comparative evidence for symmetric coupling (Scheme 9), ternary interactions (Scheme XI), and synchronous rotation (Scheme VI) are discussed in Section S3, providing a deeper understanding of their limitations.

$$r_{.BR}^{on} = r^{on} \cdot RBR_{.BR}^{on} \quad (B1)$$

$$r_{R.R}^{on} = r^{on} \cdot RBR_{R.R}^{on} \quad (B2)$$

$$r_{RB.}^{on} = r^{on} \cdot RBR_{RB.}^{on} \quad (B3)$$

las constantes reversas se obtienen

$$r_{.BR}^{off} = r^{off} \cdot RBR_{.BR}^{off} \quad (B4)$$

$$RBR_{.BR}^{off} = \frac{RBR_{.BR}^{on}}{RBR} \quad (B5)$$

An appendix contains supplementary information that is not an essential part of the text itself but which may be helpful in providing a more comprehensive understanding of the research problem or it is information that is too cumbersome to be included in the body of the paper.

References

- [1] Changeux, J.P., Devillers-Thiery, A., Chemouilli, P.: Acetylcholine receptor: an allosteric protein. *Science* **225** **4668**, 1335–45 (1984)
- [2] Nakanishi, S.: Metabotropic glutamate receptors: synaptic transmission, modulation, and plasticity. *Neuron* **13**(5), 1031–1037 (1994)

- [3] Greengard, P.: The neurobiology of slow synaptic transmission. *Science* **294**(5544), 1024–1030 (2001)
- [4] Peper, K., Bradley, R., Dreyer, F.: The acetylcholine receptor at the neuromuscular junction. *Physiological Reviews* **62**(4), 1271–1340 (1982)
- [5] Burnstock, G.: Physiology and pathophysiology of purinergic neurotransmission. *Physiological reviews* **87**(2), 659–797 (2007)
- [6] Nicke, A., Hans, B., Jürgen, R., Eichele, A., Günter, L., Ernst, M., Günter, S.: P2x1 and p2x3 receptors form stable trimers: a novel structural motif of ligand-gated ion channels. *The EMBO Journal* **17**(11), 3016–3028 (1998)
- [7] Marquez-Klaka, B., Rettinger, J., Bhargava, Y., Eisele, T., Nicke, A.: Identification of an intersubunit cross-link between substituted cysteine residues located in the putative atp binding site of the p2x1 receptor. *The Journal of Neuroscience* **27**, 1456–1466 (2007)
- [8] Hattori, M., Gouaux, E.: Molecular mechanism of atp binding and ion channel activation in p2x receptors. *Nature* **485**(7397), 207–212 (2012)
- [9] Kawate, T., Michel, J.C., Birdsong, W.T., Gouaux, E.: Crystal structure of the atp-gated p2x4 ion channel in the closed state. *Nature* **460**(7255), 592–598 (2009)
- [10] Ding, S., Sachs, F.: Single channel properties of p2x2 purinoceptors. *The Journal of General Physiology* **113**(5), 695–720 (1999)
- [11] Moffatt, L., Hume, R.I.: Responses of rat p2x2 receptors to ultrashort pulses of atp provide insights into atp binding and channel gating. *The Journal of General Physiology* **130**(2), 183–201 (2007)
- [12] Moffatt, L.: Estimation of ion channel kinetics from fluctuations of macroscopic currents. *Biophysical Journal* **93**(1), 74–91 (2007)
- [13] Hattori, M., Gouaux, E.: Molecular mechanism of atp binding and ion channel activation in p2x receptors. *Nature* **485**, 207–212 (2012)
- [14] Horrigan, F.T., Aldrich, R.W.: Coupling between voltage sensor activation, ca²⁺ binding and channel opening in large conductance (bk) potassium channels. *The Journal of General Physiology* **120**, 267–305 (2002)
- [15] Stelmashenko, O., Lalo, U., Yang, Y., Bragg, L., North, R.A., Compan, V.: Activation of trimeric p2x2 receptors by fewer than three atp molecules. *Molecular Pharmacology* **82**, 760–766 (2012)
- [16] Sattler, C., Eick, T., Hummert, S., Schulz, E., Schmauder, R., Schweinitz, A., Unzeitig, C., Schwede, F., Benndorf, K.: Unravelling the intricate cooperativity of subunit gating in p2x2 ion channels. *Scientific Reports* **10** (2020)